

**Pressure-temperature estimates of the lizardite/antigorite transition  
in high pressure serpentinites.**

Stéphane Schwartz<sup>1</sup>, Stéphane Guillot<sup>1</sup>, Bruno Reynard<sup>2</sup>, Romain Lafay<sup>1</sup>, Christian Nicollet<sup>3</sup>,  
Baptiste Debret<sup>3</sup>, Pierre Lanari<sup>1</sup>, Anne Line Auzende<sup>4</sup>

1-IsTerre, Université Grenoble 1, CNRS, F-38041 Grenoble, Cedex 9, France.

2-Laboratoire de Géologie, Ecole Normale Supérieure de Lyon, CNRS, France, Site Monod,  
15 parvis René Descartes, Lyon, F-69342, France.

3-LMV, Université Blaise Pascal, CNRS, Clermont-Ferrand, France.

4-IMPMC, Université Pierre et Marie Curie - Sorbonne Universités, 4 place Jussieu, Tour 23,  
75252 Paris Cedex 05, France.

E-mail: [stephane.schwartz@ujf-grenoble.fr](mailto:stephane.schwartz@ujf-grenoble.fr)

## Abstract

Serpentine minerals in natural samples are dominated by lizardite and antigorite. In spite of numerous petrological experiments, the stability fields of these species remain poorly constrained. This paper presents the petrological observations and the Raman spectroscopy and XRD analyses of natural serpentinites from the Alpine paleo-accretionary wedge. Serpentine varieties are identified from a range of metamorphic pressure and temperature conditions from sub-greenschist ( $P < 4$  kbar,  $T \sim 200$ - $300^{\circ}\text{C}$ ) to eclogite facies conditions ( $P > 20$  kbar,  $T > 460^{\circ}\text{C}$ ) along a subduction geothermal gradient. We used the observed mineral assemblage in natural serpentinite along with the  $T_{\text{max}}$  estimated by Raman spectroscopy of the carbonaceous matter of the associated metasediments to constrain the temperature of the lizardite to antigorite transition at high pressures. We show that below  $300^{\circ}\text{C}$ , lizardite and locally chrysotile are the dominant species in the mesh texture. Between  $320$  and  $390^{\circ}\text{C}$ , lizardite is progressively replaced by antigorite at the grain boundaries through dissolution-precipitation processes in the presence of  $\text{SiO}_2$  enriched fluids and through a solid-state transition in the cores of the lizardite mesh. Above  $390^{\circ}\text{C}$ , under high-grade blueschist to eclogite facies conditions, antigorite is the sole stable serpentine mineral until the onset of secondary olivine crystallization at  $460^{\circ}\text{C}$ .

**Keywords:** Serpentinite; Raman spectroscopy; lizardite/antigorite transition; western Alps

## 1. Introduction

Serpentine minerals are phyllosilicates that contain up to 13 wt% water and that form during the hydration of basic to ultrabasic rocks. Hydration commonly takes place in ocean spreading context, thus documenting the chemical exchanges between the oceans and solid Earth (Alt and Shanks, 2003). Serpentinities are also common in blueschist to eclogite facies terranes of oceanic or mantle wedge origin (Hattori and Guillot, 2007). Due to serpentinites' low-variance metamorphic assemblage, it is generally difficult to evaluate the P-T conditions to which they were subjected (e.g., Evans, 2004), but the associated metamorphic rocks permit approximations of the conditions. It is therefore important to accurately and rapidly characterize these common serpentine minerals. Serpentine minerals, which have simplified structure formulae  $(\text{Mg}, \text{Fe}^{2+})_3 \text{Si}_2\text{O}_5(\text{OH})_4$ , are made of superposed 1:1 alternating tetrahedral and octahedral sheets. The different spatial arrangements of these layers result in three main serpentine minerals, i.e., lizardite, chrysotile and antigorite. The sheets form flat layers in lizardite, rolls in chrysotile and curved modulated structures in antigorite (e.g., Wicks and O'Hanley, 1988). Serpentinities in high-grade metamorphic terranes indicate that antigorite is the predominant species (Scambelluri et al., 1995; Trommsdorff et al., 1998; Auzende et al., 2002; 2006; Li et al., 2004; Groppo and Compagnoni, 2007; Padron-Navarta et al., 2008; Guillot et al., 2009). Moreover, experimental studies confirm that antigorite is the stable serpentine mineral under high-pressure conditions (Ulmer and Trommsdorff, 1995; Wunder and Schreyer, 1997; Bromiley and Pawley, 2003; Perrillat et al., 2005; Komabayashi et al., 2005; Reynard and Wunder, 2006; Padron-Navarta et al., 2010). Lizardite and chrysotile are the main varieties that are present in low-grade serpentinites from the oceanic lithosphere and from low-grade metamorphic ophiolites (Evans, 2004; Andréani et al., 2007). However, the transition from low-grade to high-grade serpentine minerals is poorly constrained. Thermodynamic data predict that above 300°C, the antigorite + brucite assemblage is more stable than lizardite, and chrysotile is absent (Evans, 2004). Moreover, the antigorite + brucite assemblage is often observed in natural samples, while the chrysotile + brucite assemblage is particularly abundant in retrogressed serpentinites (Baronnet and Belluso, 2002). Thus, further petrological investigations of natural serpentinite samples, where the P-T conditions are well-constrained, are required to refine the relative stability of each variety of serpentine over a wide range of metamorphic conditions. To definitively identify serpentine varieties, transmission electron microscopy (TEM) is usually required (Mellini et al., 1995; Auzende et al., 2002; Boudier et al., 2010). Indeed, serpentine grains are only a few microns in size and

can display various habitus, which makes optical identification inaccurate. Vibrational Raman spectroscopy is also a powerful method for processing large numbers of complex samples, and numerous studies have been devoted to its use in serpentine characterization (Lewis et al., 1996; Bard et al., 1997; Klopogge et al., 1999; Rinaudo et al., 2003; Auzende et al., 2004; Groppo et al., 2006). In particular, the region of the OH stretching vibrational modes can be conveniently used to discriminate among the different varieties of serpentine (Auzende et al., 2004). The OH stretching modes in the high wavenumber range (approximately 3500 cm<sup>-1</sup>) of the different serpentines are tentatively described in terms of the curvature of the layers, with potential applications for structural characterization by Raman spectroscopy. Raman spectroscopy permits the characterization of the phases at a micrometer scale of bulk samples or thin sections. To assess the reliability of Raman spectroscopy for identification purposes, we apply it to serpentines in a series of low to high pressure metamorphic serpentinite samples from the western Alps for which TEM characterization have been independently performed (Auzende et al., 2006). The serpentinites are also characterized by XRD in order to decipher the bulk serpentinite mineralogy.

## **2. Geological setting**

Alpine evolution along the Eurasia-Africa boundary was initially dominated by plate divergence, which induced Mesozoic rifting and oceanic opening. Since Cretaceous time, the plate convergence has resulted in subduction and collision (Rosenbaum and Lister, 2005; Dumont et al., 2012). This study focuses on the Piedmont zone of the southwestern Alps (Figs 1a and 1b), which is composed of the association of units that originated in the distal European margin and from the nearby oceanic domain (Lemoine et al., 1986) and that were juxtaposed during the subduction and collision in Late Cretaceous to Tertiary times (Tricart, 1984). The Piedmont zone includes different levels of the paleo-subduction zone, preserving the low thermal gradient (5-8 °C/km) associated with the subduction dynamics; moreover, it is partially overprinted by Alpine metamorphism conditions (Schwartz et al., 2001, 2007, Agard et al., 2002). At the top of the nappe pile, the Chenaillet massif corresponds to an obducted portion of the Tethyan oceanic lithosphere. This unit rests upon the Queyras Schistes lustrés (Fig. 1c), which represents a fossiliferous sedimentary accretionary wedge developed under blueschist facies conditions during the late Cretaceous–early Eocene subduction of the Tethyan Ocean (Schwartz, 2000; Tricart and Schwartz, 2006; Schwartz et al., 2009), as previously indicated by structural observations further to the north in the same Piedmont zone (Agard et al., 2001; Ganne et al., 2005). This domain derived from Mesozoic

oceanic sediments that were primarily composed of metamorphic marls, clays, and limestones (calcschists). These sediments were strongly deformed and metamorphosed during alpine subduction, and they outcrop today as foliated and polydeformed calcschists enclosing boudinaged meter- to kilometer-sized Jurassic ophiolites (Tricart and Lemoine, 1986; Lagabrielle and Polino, 1988). The P-T conditions increase towards the east, from low temperature-blueschist facies conditions (LT-blueschist) in western Queyras to the transitional conditions between high-temperature blueschist (HT-blueschist) and eclogite facies in eastern Queyras (Agard et al., 2001; Tricart and Schwartz, 2006; Schwartz et al., 2009). This blueschist domain is structurally above the Monviso eclogitic ophiolite. In this massif, the metasedimentary component is very small (< 20 vol.%) relative to the voluminous oceanic lithosphere (Schwartz et al., 2001). The serpentinite bodies are located along detachments and constitute a large volume of the eastern boundary of the massif (Schwartz et al., 2001, Angiboust et al., 2012). The Monviso ophiolite corresponds to the subduction channel (Guillot et al., 2009).

### 3. Sampling strategy

The Chenaillet-Queyras-Monviso transect is a unique natural laboratory for observing mineral changes in serpentinite along an increasing metamorphism gradient. However, there are no directly applicable thermal calibrations in serpentinites; therefore, we propose to estimate the thermal conditions by applying the method of Raman spectroscopy of carbonaceous material (RSCM) to the metasediments associated with the serpentinites to obtain the  $T_{\max}$  experienced by the serpentinites. A thermal transect is realized, according to 25 metasediment samples from the Chenaillet to the Monviso (Fig. 1a, Table 1). These sediments are Cretaceous calcschists derived from foraminifera oozes (Deville et al., 1992). The lithology of each sample is not homogeneous due to the variation in carbonate-clay proportions. Moreover, the carbonate contents result both from biogenic production (pelagic foraminifera) and from detrital input (calciturbidites). The samples are strongly deformed, and the main schistosity is dominated by phengite, quartz, calcite and oxides. Glaucophane and pseudomorphs of lawsonite and zoisite are also present. Along this thermal transect, 7 serpentinites have been studied (Fig. 1a). The serpentinite samples were taken from the cores of hecto-metric serpentinite bodies; these bodies were embedded in the metasediments from which the metasediment samples were acquired. These serpentinites escaped alpine deformations and preserved the oceanic mesh textures. Sample ICH2 comes from the ophiolitic Chenaillet massif. This sample records a low degree of metamorphic conditions,

with sea-floor metamorphism (Mével et al., 1978) overprinted by sub-greenschist facies conditions ( $P < 4$  kbar;  $T \sim 200\text{-}300^\circ\text{C}$ ; Goffé et al., 2004) related to alpine metamorphism. Sample CR02 comes from the Cristillan massif at the western boundary of the Schistes lutrés complex in the LT-blueschist domain (Fig. 1). Two samples come from the medium-temperature blueschist domain (MT-blueschist) of the Schistes lutrés complex: RQ23 from the Rocca Nera massif and RQ16 from the Eychassier massif. Samples BB01 (Bric Bouchet massif) and RQ01 (Traversette massif) come from the HT-blueschist domain of the Schistes lutrés complex. The final sample, Vi01, comes from the Monviso eclogitic ophiolite.

## **4. Temperature estimates from Raman spectroscopy of carbonaceous material (RSCM)**

### **4.1. Analytical conditions**

Raman spectroscopy on carbonaceous material (RSCM) is based on the quantitative degree of graphitization of the organic material during regional metamorphic processes. The graphitization phenomenon corresponds to the solid-state transformation of organic matter into carbonaceous material. The structure of carbonaceous matter is not sensitive to the retrograde history related to the exhumation of metamorphic rocks. The progressive graphitization process can be used to estimate the peak temperature ( $T_{\text{max}}$ ) reached by a given sample (Beyssac et al., 2002, 2003). The degree of graphitization appears to be independent of the metamorphic pressure, although a minimum pressure is required for the graphitization process to take place (Quirico et al., 2009). This thermometer is based on the quantification of the degree of ordering of the carbonaceous material, using the R2 area ratio between the G, D1 and D2 bands ( $R2 = D1/[G+D1+D2]$ ) extracted from the Raman spectra (Beyssac et al., 2002). The R2 ratio is linearly correlated with the  $T_{\text{max}}$  of the metamorphic cycle ( $T_{\text{max}}(^{\circ}\text{C}) = -445 \times R2 + 641$ ). This correlation may be used as a thermometer with an intrinsic error calibration of  $50^\circ\text{C}$  due to the petrological data used for calibration and a relative accuracy of approximately  $15^\circ\text{C}$  (Beyssac et al., 2007).

Raman spectroscopy was performed at the ENS-Lyon using a Horiba Jobin-Yvon LabRam HR800 apparatus. The excitation was realized by an argon laser with a wavelength of 514 nm. An Olympus<sup>TM</sup> BX30 open microscope equipped with a  $\times 100$  objective lens was coupled to the spectrometer to focus the laser beam onto an area that was 1  $\mu\text{m}$  in diameter. The backscatter of the Raman signal was collected. The acquisition duration was

approximately 120 s distributed over two accumulating cycles, with a laser power of approximately 700  $\mu$ W at the sample surface. The signal was dispersed using a 1800 lines/mm grating. The Raman spectrometer was calibrated with a silicon standard. For each sample, 11 to 13 spectra were recorded (noted 'n' in Table 1). The baseline correction, peak position, and band width were determined using the Peakfit© software.

#### 4.2. $T_{\text{max}}$ results

From west to east, the Raman spectra show a decrease of the D1 peak area associated with a decrease in the width of the G band, resulting in a decrease of the R2 ratio (Fig. 1b). This trend in the R2 ratio is compatible with a  $T_{\text{max}}$  increase in the metamorphic samples (Beyssac et al., 2007; Lanari et al., 2012). The  $T_{\text{max}}$  estimates by RSCM thermometry range from  $330 \pm 20^\circ\text{C}$  to  $520 \pm 20^\circ\text{C}$  (Table 1). The projection of the estimated  $T_{\text{max}}$  along a WSW to ENE profile (XX' in Fig. 1c) shows a progressive increase of  $T_{\text{max}}$ . This increase in temperature is compatible with the metamorphic gradient already proposed by Tricart and Schwartz (2004) in the studied area. The temperature increase from west to east is also consistent with the increase in pressure along a low-temperature subduction-related geothermal gradient (Goffé et al., 2004; Lardeaux et al., 2006; Angiboust et al., 2012). This relationship allows us to associate a pressure maximum with the  $T_{\text{max}}$  estimated by RSCM. The sub-greenschist facies domain of the Chenaillet massif corresponds to a P-T range of  $P < 4$  kbar and  $T \sim 200\text{-}300^\circ\text{C}$ . The LT-blueschist domain corresponds to P-T conditions of  $P = 9\text{-}11$  kbar and  $320 < T < 360^\circ\text{C}$ ; the MT-blueschist domain indicates P-T conditions of  $10\text{-}12$  kbar and  $340\text{-}390^\circ\text{C}$ ; the HT-blueschist domain corresponds to P-T conditions of  $12 < P < 15$  kbar and  $380 < T < 470^\circ\text{C}$ ; and the eclogitic domain indicates conditions of  $20 < P < 26$  kbar and  $480 < T < 520^\circ\text{C}$ .

## 5. XRD serpentinites characterization

### 5.1. Experimental conditions

The  $< 2$  mm fraction of the serpentinite samples was powdered using a McCrone micronizing mill and washed with  $\text{H}_2\text{O}$ . The resulting slurry was centrifuged and freeze-dried before being prepared as a randomly oriented mount. The XRD patterns were recorded with a Bruker D5000 powder diffractometer equipped with a SolX Si(Li) solid state detector from Baltic Scientific Instruments using  $\text{CuK}\alpha$  1+2 radiation. The intensities were recorded at

0.04° 2-theta step intervals from 5 to 90° (5 s counting time per step) for bulk serpentinite mineralogy determination. The XRD detection level was approximately one percent (< 1%).

## 5.2. Results

The XRD results and the mineralogical assemblages are presented in Figure 2 and Table 2. All of the XRD lines of the samples are dominated by serpentine minerals (serpentine species > 90%) associated with magnetite (Fig. 2). Brucite is not observed; however, mineral species are not detected below a concentration of 1 wt%. The serpentinite sampled in the Chenaillet massif (ICH2) is composed of serpentine, magnetite, chlorite and rare magmatic clinopyroxene. The serpentinites sampled in the LT-blueschist (CR02) and MT-blueschist (RQ23 and RQ16) domains present mineralogical assemblages dominated by serpentine and minor magnetite. In Sample RQ16, chlorite is detected. The serpentinites from the HT-blueschist (BB01 and RQ01) and eclogitic (Vi01) domains are composed of serpentine, metamorphic olivine and magnetite. The mineral antigorite is detectable in the XRD spectrum of Sample BB01 (Fig. 2 and Table 2). The presence of olivine is related to the onset of antigorite destabilization during the dehydration reaction (Evans, 2004). This secondary olivine appears in Samples RQ01 and Vi01. In Sample Vi01, clinopyroxene and chlorite are detected, in accordance with the microscopic observations (Auzende et al., 2006). To precisely identify the varieties of serpentines, we used Raman spectroscopy coupled with microscopic observations.

## 6. Serpentine characterizations

### 6.1. Raman spectrometry

The different serpentine species have been characterized by Raman spectroscopy coupled with petrographic observations of polished thin-sections of serpentinites. The Raman signal was acquired over approximately 90 s in three accumulating cycles, with a laser output power on the sample surface adjusted between 10 and 20 mW. The spectral resolution was 1 cm<sup>-1</sup> using 1800 lines/mm grating. A reproducibility of 1 cm<sup>-1</sup> was attained on successive spectra of a given mineral sample. The spectral regions from 150 to 1150 cm<sup>-1</sup> and from 3600 to 3720 cm<sup>-1</sup> were investigated because they include the lattice vibrational modes and the OH stretching mode region that is characteristic of serpentine species, respectively (Rinaudo et al., 2003; Auzende et al., 2004; Groppo et al., 2006).



The bands detected in these spectral regions are indicative of the crystalline structure of the sample. For each spectra, the assignment of the band position and the full width at half maximum were determined using the Peakfit© software.

In the low wavenumber region, four main peaks (near 230, 390, 690 and 1100  $\text{cm}^{-1}$ ) characterize the spectra of lizardite and chrysotile (Fig. 3a). Intense peaks specific to the antigorite spectrum occur at lower wavenumbers (226, 373, 680 and 1043  $\text{cm}^{-1}$ ) and are much broader than those corresponding to other serpentines (Fig. 3b). The differences between chrysotile and lizardite spectra, although small, can be clearly identified by the sharpness of the Raman lines. In particular, a single band at 1100  $\text{cm}^{-1}$  is observed in chrysotile, whereas several convoluted bands are observed between 1060 and 1100  $\text{cm}^{-1}$  in lizardite (Fig. 3a). In the high wavenumber region, the convoluted vibrational modes attributed to the OH stretching of serpentine are located between 3600 and 3720  $\text{cm}^{-1}$ . In chrysotile, the most intense band occurs at 3697  $\text{cm}^{-1}$ , with a distinct shoulder at 3690  $\text{cm}^{-1}$  and a weak band at 3648  $\text{cm}^{-1}$ . Lizardite has a markedly different spectrum (Fig. 3a): the most intense band occurs at a lower frequency (minimum at 3680  $\text{cm}^{-1}$ ) with a well-defined high frequency band at 3703  $\text{cm}^{-1}$ . In antigorite, the spectra are characterized by a broad band at 3670  $\text{cm}^{-1}$  and a sharp band at 3700  $\text{cm}^{-1}$  (Fig. 3b). Mixed lizardite/antigorite spectra are also observed (Fig. 3c). In the low wavenumber region, the peak at 1043  $\text{cm}^{-1}$  is present (as in antigorite), but the peak at 373  $\text{cm}^{-1}$  is shifted to  $\sim 380 \text{ cm}^{-1}$  (toward the classical  $\sim 390 \text{ cm}^{-1}$  peak of lizardite). In the high wavenumber region, the second “antigorite” peak at 3700  $\text{cm}^{-1}$  is still present, but the most intense peak is located between 3670  $\text{cm}^{-1}$  and 3680  $\text{cm}^{-1}$ , in an intermediate position between the most intense “antigorite” and “lizardite” peaks (Fig. 3c).

## 6.2. Petrology

The repartition of the serpentine species correlates with the  $T_{\text{max}}$  along the XX' profile (Fig. 1c). Lizardite dominates in the greenschist and LT-blueschist facies (from  $< 300^\circ\text{C}$  to  $360^\circ\text{C}$ ), while antigorite progressively appears in the LT-blueschist facies. Antigorite becomes progressively dominant in the MT-blueschist facies ( $340\text{--}390^\circ\text{C}$ ), ultimately becoming the sole serpentine species in the HT-blueschist and eclogite facies ( $T > 380^\circ\text{C}$ ). Chrysotile is observed in all of the high pressure serpentinite samples, filling in the late cracks or micro-fractures related to the samples' final exhumation at the ductile/brittle transition. In the following paragraphs, we detail the mineralogy and texture of the serpentinites according

to the degree of metamorphism. The  $T_{\max}$  for each serpentinite sample refers to the  $T_{\max}$  estimated from the associated metasediments.

Sample ICH2 ( $T < 300^{\circ}\text{C}$ ) is characterized by the development of a mesh texture underlined by magnetite, which suggests the classical reaction of olivine + water = serpentine (mesh) + magnetite  $\pm$  brucite (Figs 4a and 4a'). The Raman spectrometry shows that lizardite is the dominant serpentine species. Locally, the mesh is crosscut by secondary chrysotile veins.

Sample CR02 ( $T_{\max} = 340^{\circ}\text{C}$ ) shows a mesh texture consisting of lizardite surrounded by magnetite (Figs 4b and 4b'). Locally, secondary antigorite (representing less than 10% of the matrix) crystallized at the boundaries of relict brownish lizardite crystals. We assign the lizardite crystallization to the sea-floor metamorphism (oceanic serpentinization) and the antigorite crystallization to the LT-blueschist metamorphism.

Sample RQ23 ( $T_{\max} = 356^{\circ}\text{C}$ ) is equally composed of antigorite and relics of lizardite (Figs 4c and 4c'). The antigorite crystallized at the grain boundaries of the lizardite relics and as millimeter-sized antigorite patches with an interlocking texture. The lizardite relics present the typical mixed lizardite-antigorite Raman spectra, suggesting the partial mineral replacement of oceanic lizardite by metamorphic micrometric antigorite. Magnetite locally underlines the original mesh texture.

Sample RQ16 ( $T_{\max} = 373^{\circ}\text{C}$ ) shows the same mineral relationship as Sample RQ23, with some relics of lizardite that have a mixed character between antigorite and lizardite (Figs 4d and 4d'). The antigorite that developed at the grain boundaries enlarged and the blades of antigorite crystallized. In this sample, the proportion of magnetite decreased, but chlorite crystallized (Fig. 2), which suggests the development of chlorite at the expense of magnetite in the presence of aluminum.

Sample BB01 ( $T_{\max} = 402^{\circ}\text{C}$ ), coming from the HT-blueschist unit, is composed only of antigorite and a string of magnetite that underlies the previous oceanic mesh texture (Figs 5a and 5a'). The patches are composed of sub-millimetric interlocking blades of antigorite. The presence of antigorite is readily detectable in the XRD spectra (Fig. 2).

In Sample RQ01 ( $T_{\max} = 463^{\circ}\text{C}$ ), only antigorite serpentine is observed (Figs. 5b and 5b'). The mesh, still underlined by magnetite and bastite (free of magnetite), remains preserved, which suggests a static crystallization of antigorite at the expense of oceanic lizardite. The olivine peak appears in the XRD spectra.

In Sample Vi01 ( $T_{\text{max}} = 498^{\circ}\text{C}$ ), antigorite is again the sole serpentine species (Figs. 5c and 5c'). Similar to Sample RQ01, the pseudomorphic texture (mesh and bastite) is preserved and underlined by magnetite, but antigorite blades of a few hundred microns have started to obliterate the mesh texture. In this sample, we observed olivine and chlorite signals in the XRD spectra (Fig. 2).

### 6.3. Electron microprobe

In addition, the major element concentrations of the serpentine species were acquired using a Cameca SX100 electron microprobe at the “Laboratoire Magma et Volcans” (Clermont Ferrand, France). The operating conditions were as follows: an accelerating voltage of 15 kV, a sample current of 15 nA and a counting time of 10 s/element, except for Ni (20 s). The standards used were albite (Na), forsterite (Mg), orthoclase (K), wollastonite (Ca and Si),  $\text{MnTiO}_3$  (Ti and Mn),  $\text{Cr}_2\text{O}_3$  (Cr), fayalite (Fe), olivine (Ni), and synthetic  $\text{Al}_2\text{O}_3$  (Al). Representative analyses are reported in Table 3. Serpentine phases can contain over 13 wt% of water in their crystal structure. The volatile content is not always correlated with the degree of serpentinization because other phases (e.g., talc, brucite, chlorite, clay minerals) associated with serpentine minerals can influence this measurement. In the studied samples, the volatile content (100% – wt% major elements) varies from 12.54 to 15.67 wt% (Table 3). We did not observe any correlation between the volatile content in the serpentine minerals and the degree of metamorphism. However, we did observe a relationship between the homogenization of the serpentine composition and the degree of metamorphism (Fig. 6). When plotted on the  $\text{SiO}_2$  vs.  $\text{Al}_2\text{O}_3$  field, the lower metamorphic samples are scattered, while the higher metamorphic samples are grouped closer to the end-member antigorite composition (Fig. 6), with 44 wt%  $\text{SiO}_2$  and 1.03 wt%  $\text{Al}_2\text{O}_3$  (Deer et al., 1992). The samples with an intermediate degree of metamorphism, dominated by mixed lizardite/antigorite, fall between the lizardite and antigorite fields. It is also noticeable that the  $\text{Al}_2\text{O}_3$  content decreases and the  $\text{SiO}_2$  content increases with the degree of metamorphism (Fig. 6). This increase of  $\text{SiO}_2$  in serpentine is correlated with a slight increase of whole-rock  $\text{SiO}_2$  content, from ~39.4 wt% at grade 0 to ~40.5 wt% (Lafay et al., in press).

## 7. Discussion

### 7.1. Lizardite to antigorite transitions

The aim of this study is to develop a combined mineral investigation of serpentinites and compare the results with  $T_{\text{max}}$  estimates from associated metasediments. This approach allows us to indirectly constrain the P-T conditions of the phase changes in natural serpentinites and to compare our results with previous experimental works. Moreover, most of the published results concerning the changes from lizardite/chrysotile to antigorite are acquired through experiments performed at intermediate pressures of approximately 6-7 kbar (e.g., O'Hanley (1996); our samples allow us to characterize this transition at higher pressures (between 4 and 26 kbar) that are pertinent to the P-T conditions in subduction zones. Our study highlights the following important points:

1-The early serpentinization stage is related to the hydrothermalism of the oceanic lithosphere and generates lizardite-bearing mesh textures (Figs. 7a and 7b).

2-In the lowest-grade metamorphic units (sub-greenschist facies;  $P < 4$  kbar;  $T \sim 200$ - $300^{\circ}\text{C}$ ), antigorite is absent and lizardite is the dominant phase. Such observations are in agreement with previous experimental results (e.g., Evans, 2004).

3-In polymetamorphic weakly deformed domains, the oceanic mesh textures are preserved in all peak P-T conditions (Fig. 7b). At the initial stages, antigorite appears along the lizardite grain boundaries (Fig. 7c) and at more evolved stages overprints lizardite (Fig. 7d), preserving the initial textures (mesh and bastite). This observation argues against the commonly proposed idea that antigorite preferentially crystallizes within deformed domains (Miyashiro et al., 1969).

4-Antigorite crystallizes in two distinct crystallographic sites. Antigorite first appears in LT-blueschist at  $320^{\circ}\text{C}$  at the lizardite grain boundary, forming a network of veins (Fig. 7c). These veins grow with the degree of metamorphism, from  $\sim 20 \mu\text{m}$  up to  $150 \mu\text{m}$  (Fig. 7d) in the MT-blueschist facies (up to  $390^{\circ}\text{C}$ ). Such crystallization texture is typical of mineral replacement by dissolution-precipitation processes in the presence of a free fluid (Putnis, 2009; Lafay et al., 2012).

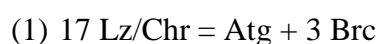
The second crystallographic site is where antigorite crystallizes in the cores of lizardite grains in MT-blueschist facies conditions (Fig. 7d). Raman spectrometry shows mixed lizardite/antigorite spectra, suggesting an intimate association of lizardite and antigorite at the micron-scale (Fig. 7a). This intimate mineral association suggests a solid-state transition (Eda et al., 2006). The solid-state crystallization of antigorite at the expense of lizardite is partial

between 340 and 380°C and complete above in HT-blueschist and eclogitic facies conditions (Figs. 7a and 7e).

## 7.2. Lizardite to antigorite reactions

In the literature, it is typically proposed that the thermal stability fields of antigorite and lizardite overlap between temperatures of 250 and 500°C, while chrysotile is metastable (e.g., Evans, 2004). We can refine the relative stability fields of lizardite and antigorite from our observations of high-pressure natural samples. It is well known that serpentinization is a complex process controlled by time- and site-dependent variables such as fluid/rock ratios, silica activity, oxygen fugacity and pH (Evans, 2004; Frost and Beards, 2007). Lizardite and antigorite are co-stable (or at least the lizardite is not completely destabilized) between 320 and 390°C for pressures greater than 9 kbar (Fig. 7). It is noticeable that below 300°C and 4 kbar, antigorite is not observed. This observation contradicts the phase diagram of O'Hanley (1996), in which antigorite appears at 250°C at low pressures, and suggests that antigorite crystallization is not only temperature dependent but also may be pressure dependent (Ulmer and Trommsdorff, 1995; Wunder and Schreyer, 1997).

Thermodynamic work on the serpentinite multisystem predicts the crystallization of antigorite (Atg) at the expense of chrysotile (Chr) or lizardite (Lz), according to the following reactions (Evans, 2004) with forsterite (Fo) and brucite (Brc):

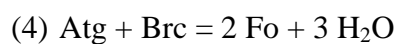


Reactions (1) and (2) are thermodynamically favorable for temperatures between 300 and 400°C (Fig. 8), while at lower temperatures, the conversion of lizardite to antigorite is thermodynamically more efficient with a modest introduction in the serpentinite multisystem of SiO<sub>2</sub> (e.g., Evans, 2004). Brucite is not detected as a byproduct of antigorite; however, we can conclude that brucite is not present in the studied samples below the XRD concentrations (< 1 wt%), although brucite is detected in the Monviso serpentinites (Debret, pers. com.). The absence of brucite could be interpreted either as the result of a lower olivine hydration with respect to enstatite hydration (precluding the release of Mg necessary to the brucite crystallization) or as the consumption of brucite during prograde reactions. Metamorphic

olivine is rare and observed in the studied samples at temperatures higher than 460°C. Thus, Reactions (1) and (2) cannot explain the crystallization of antigorite at low temperatures (< 330°C according to Evans (2004)). In contrast, we clearly observe the direct crystallization of veins of antigorite at the expense of lizardite starting at 320°C in the presence of metasediments. Moreover, we observe a general enrichment in SiO<sub>2</sub> throughout the antigorite (Fig. 6) that is correlated with a whole-rock SiO<sub>2</sub> enrichment along the metamorphic gradient (Lafay et al., in press). This finding suggests the onset of antigorite crystallization at 320°C, assisted by SiO<sub>2</sub>-rich fluids, according to Reaction (3), by dissolution-precipitation processes (Fig. 8). Rüpke et al. (2004) have shown that above a depth of 50 km (T < 300°C), oceanic sediments release almost 50% of their initial water content. This fluid is enriched in volatile elements and silica and potentially hydrated the mantle wedge (e.g., Bebout and Barton, 1989; Bebout et al., 1999). Fluid exchange between the subducted oceanic sediments and our serpentinite samples is clearly demonstrated by the enrichment of volatile elements, particularly in the antigorite (Lafay et al., in press). Thus, the most favorable circumstances for silicification are waters that are equilibrated with sedimentary rocks in the Alpine wedge and that percolated into the serpentinites, as observed in the Catalina Schist in California (Bebout and Barton, 1989, Bebout et al., 2004).

As already discussed, we also observed the solid-state transformation of lizardite into antigorite, suggesting the progression of Reaction (1) between 340 and 380°C. In the natural samples presented here, this reaction occurred at slightly higher temperatures than were predicted by thermodynamic calculations (260-310°C at 10 kbar, Evans, 2004).

At a minimum temperature of 460°C, secondary olivine crystallized (Fig. 2), which suggests the onset of antigorite destabilization. This is compatible with a decrease of the whole-rock L.O.I from 13 wt% to < 12 wt% (Lafay et al., in press). According to Evans (2004), it corresponds to the reaction:



In the natural samples studied, this reaction occurred at  $\geq 460^\circ\text{C}$  and  $P > 12 \text{ kbar}$ , as predicted by thermodynamic calculations (Evans, 2004). However, this reaction involves brucite, which we did not detect in the samples. Thus, we propose that the brucite produced by Reaction (1) at lower temperatures is completely consumed by Reaction (4) along the subduction gradient (Fig. 8).

## 8. Conclusion

Raman spectroscopy and XRD are efficient methods for identifying different species of serpentine because serpentine optical identification is difficult. In addition, various serpentine species are often interpenetrated, and Raman micro-spectrometry proves to be a useful micro-characterization tool for resolving structural differences at the scale of the various grain generations. The application of these methods to samples from the Alps shows that lizardite is preserved under sub-greenschist facies conditions in oceanic environment and ophiolites. Antigorite progressively replaces lizardite under LT- to MT-blueschist facies conditions (320-390°C) and is the sole serpentine phase under HT-blueschist to eclogites facies conditions (> 380°C). Our study shows several generations of serpentine in sea-floor and metamorphic processes. Below 320°C, lizardite and chrysotile are the only stable serpentine species. Between 320°C and 390°C, lizardite and antigorite coexist and antigorite develops at the expense of lizardite through two processes. Antigorite first appears at the lizardite grain boundaries through dissolution-precipitation processes in the presence of SiO<sub>2</sub>. We propose that this fluid comes from the local dehydration of the surrounding metasediments in subduction environments. Antigorite also crystallizes in the cores of the lizardite mesh through solid-state transitions at slightly higher temperatures, between 340°C and 380°C. This transition is characterized by mixed lizardite/antigorite Raman spectra. Above 390°C and 12 kbar, lizardite is absent and antigorite is the only stable serpentine species. Above 460°C, antigorite begins to destabilize into olivine. We did not detect brucite in any of the studied samples, although this mineral is theoretically involved in the transition from lizardite to antigorite. We propose that the brucite produced at low temperatures is consumed at higher temperatures and remains a transition phase. This process would explain why brucite is rarely observed in natural samples in oceanic and subduction environments worldwide.

## 9. Acknowledgments

This study was supported by the *Agence Nationale de la Recherche* project n° ANR-08-BLAN-0303-01 “Erosion and Relief Development in the Western Alps”, the SUBDEF grant n° ANR-08-BLAN-0192 and the Labex OSUG2020. N. Findling is thanked for the XRD analyses (University of Grenoble 1).

## 10. References

- Agard, P., Monié, P., Jolivet, L., and Goffé, B., 2002. Exhumation of the Schistes Lustrés complex: In situ laser probe Ar-40/Ar-39 constraints and implications for the western Alps. *Journal of Metamorphic Geology* 20, 599-618.
- Agard, P., Vidal, P., Goffé, B., 2001. Interlayer and Si content of phengite in HP-LT carpholite-bearing metapelites. *Journal of Metamorphic Geology* 19, 479-495.
- Alt, J.C., Shanks, W.C., 2003. Serpentinization of abyssal peridotites from the MARK area, Mid-Atlantic ridge, sulphur geochemistry and reaction modelling. *Geochimica Cosmochimica Acta* 67, 641-653.
- Andréani, M., Mével, C., Boullier, A.M., Escartin, J., 2007. Dynamic control on serpentine crystallisation in veins: constraints on hydration processes in oceanic peridotites. *Geochemistry Geophysics Geosystems* Q02012, doi: 10.1029/2006GC001373.
- Angiboust, S., Langdon, R., Agard, P., Waters, D., Chopin C., 2012. Eclogitization of the Monviso ophiolite (W. Alps) and implications on subduction dynamics. *Journal of Metamorphic Geology* 30, 37-61.
- Auzende, A.L., Guillot, S., Devouard, B., Baronnet, A., 2006. Serpentinites in Alpine convergent setting: Effects of metamorphic grade and deformation on microstructures. *European Journal of Mineralogy* 18, 21-33.
- Auzende, A.L., Daniel, I., Reynard, B., Lemaire, C., Guyot, F., 2004. High-pressure behaviour of serpentine minerals: a Raman spectroscopic study. *Physics and Chemistry of Minerals* 31(5), 269-277.
- Auzende, A.L., Devouard, B., Guillot, S., Daniel, I., Baronnet, A., Lardeaux, J.M., 2002. Serpentinites from Central Cuba: petrology, and HRTEM study. *European Journal of Mineralogy* 14, 905-914.
- Bard, D., Yarwood, J., Tylee, B., 1997. Asbestos fibre identification by Raman microspectroscopy. *Journal of Raman Spectroscopy* 28, 803-809.
- Baronnet, A., Belluso, E., 2002. Microstructures of the silicates: key information about mineral reactions and a link with the Earth and materials sciences. *Mineralogical Magazine* 66, 709-732.
- Bebout, G.E., Ryan, J.G., Leeman, W.P., Bebout, A.E., 1999. Fractionation of trace elements by subduction-zone metamorphism, effect of convergent-margin thermal evolution. *Earth and Planetary Science Letters* 171, 63-81.
- Bebout, G.E., Barton, M.K., 1989. Fluid flow and metasomatism in a subduction zone hydrothermal system: Catalina Schist terrane, California. *Geology* 17, 976-980.



477 Beyssac, O., Goffé, B., Chopin, C., Rouzaud, N., 2002. Raman spectra of carbonaceous  
478 material in metasediments : a new geothermometer. *Journal of Metamorphic Geology* 20,  
479 859-871.

480 Beyssac, O., Goffé, B., Petitet, J.P., Froigneux, E., Moreau, M., Rouzaud, J.N., 2003. On the  
481 characterisation of disordered and heterogeneous carbonaceous materials by Raman  
482 spectrometry. *Spectrochimica Acta* 59, 2267-2276.

483 Beyssac, O., Simoes, M., Avouac, J.P., Farley, K.A., Chen Y.G., Goffé, B., 2007. Late  
484 Cenozoic metamorphic evolution and exhumation of Taiwan. *Tectonics* 26 TC6001, pp. 32.

485 Boudier, F., Baronnet, A., Mainprice, D., 2010. Serpentine mineral replacements of natural  
486 olivine and their seismic implications : oceanic lizardite versus subduction-related antigorite.  
487 *Journal of Petrology* 51, 495-512.

488 Bromiley, G.D., Pawley, A.R. 2003. The stability of antigorite in the systems MgO-SiO<sub>2</sub>-H<sub>2</sub>O  
489 (MSH) and MgO-Al<sub>2</sub>O<sub>3</sub>-SiO<sub>2</sub>-H<sub>2</sub>O (MASH): The effects of Al<sup>3+</sup> substitution on high-pressure  
490 stability. *American Mineralogist* 88, 99-108.

491 Deer, W.A., Howie, R.A., Zussman, J., 1992. An introduction to the rock-forming minerals,  
492 2nd edition. Longman Scientific & Technical, Harlow.

493 Deville, E., Fudral, S., Lagabriele, Y., Marthaler, M., Sartori, M., 1992. From oceanic closure  
494 to continental collision: A synthesis of the Schistes lustrés metamorphic complex of the  
495 western Alps. *Geological Society of America Bulletin* 104, 127-139.

496 Dumont T., Schwartz S., Guillot S., Simon-Labrie T., Tricart P., Jourdan S., 2012. Structural  
497 and sedimentary records of the Oligocene revolution in the Western Alps. *Journal of*  
498 *Geodynamics* 56-57, 18-38.

499 Eda, K., Uno, Y., Nagai, N., Sautani, N., Chen, C., Whittingham, M.S., 2006. Structure-  
500 inheriting solid-state reactions under hydrothermal conditions. *Journal of Solid State*  
501 *Chemistry* 179, 1453-1458.

502 Evans, B.W., 2004. The Serpentinite Multisystem Revisited: Chrysotile is Metastable.  
503 *International Geology Review* 46, 479-506.

504 Frost, B.R., Beard, J.S., 2007. On silica activity and serpentinization. *Journal of Petrology* 49,  
505 1351-1368.

506 Ganne, J., Bertrand, J.M., and Fudral, S., 2005. Fold interference pattern at the top of  
507 basement domes and apparent vertical extrusion of HP rocks (Ambin and South Vanoise  
508 massifs, western Alps). *Journal of Structural Geology* 27, 553-570.

509 Goffé, B., Schwartz, S., Lardeaux, J.M., Bousquet, R., 2004. Metamorphic structures of the  
510 Western and Ligurian Alps. *Mitteilungen der Österreichischen Mineralogischen Gesellschaft*  
511 149, 125-144.

512 Groppo, C., Compagnoni, R., 2007. Metamorphic veins from the serpentinites of the  
513 Piemonte Zone, western Alps, Italy: a review. *Periodico di Mineralogia* 76, 127-153.

514 Groppo, C., Rinaudo, C., Cairo, S., Gastaldi, D., Compagnoni, R., 2006. Micro-Raman  
515 spectroscopy for quick and reliable identification of serpentinite minerals from ultramafics.  
516 *European Journal of Mineralogy* 18, 319-329.

517 Guillot, S., Hattori, K., Agard, P., Schwartz, S., Vidal, O., 2009. Exhumation processes in  
518 oceanic and continental subduction contexts: a review. In S. Lallemand and F. Funiciello  
519 (eds.) "Subduction Zone Dynamics", Springer-Verlag Berlin Heidelberg. doi: 10.1007/978-3-  
520 540-87974-9, 175-204.

521 Hattori, K., Guillot, S., 2007. Geochemical character of serpentinite associated with high to  
522 ultrahigh pressure rocks in Alps, Cuba and the Himalayas: recycling of elements in  
523 subduction zones. *Geochemistry Geophysics Geosystems* Q09010,  
524 doi:10.1029/2007GC001594.

525 Kloprogge, J.T., Frost, R.L., Rintoul, L., 1999. Single crystal Raman microscopic study of the  
526 asbestos mineral chrysotile. *Journal of Physical Chemistry* 1, 2559-2564.

527 Komabayashi, T., Hirose, K., Funakoshi, K., Takafuji, N., 2005. Stability of phase A in  
528 antigorite (serpentine) composition determined by in situ X-ray pressure observations. *Physics*  
529 *of the Earth and Planetary Interiors* 151, 276-289.

530 Lanari P., Guillot S., Schwartz S., Vidal O., Tricart P., Riel N., Beyssac O., 2012.  
531 Diachronous evolution of the alpine continental wedge: evidences from P-T estimates in the  
532 Briançonnais Zone houillère (France-Western Alps). *Journal of Geodynamics* 56-57, 39-54.

533 Lagabrielle, Y., and Polino, R., 1988. Un schéma structural du domaine des Schistes lustrés  
534 ophiolitifère au nord-ouest du massif du Mont Viso (Alpes Sud-Occidentales) et ses  
535 implications. *Comptes Rendus de l'Académie des Sciences* 306, 921-928.

536 Lafay, R., Montes-Hernandez, G., Janots, E., Chiriac, R., Findling, N., Toche, F., 2012.  
537 Mineral replacement rate in olivine by chrysotile and brucite under high alkaline conditions.  
538 *Journal of Crystal Growth* 347, 62-72.

539 Lafay R., Deschamps F., Schwartz S., Guillot S., Godard M., Nicollet C. High-pressure  
540 serpentinites, a trap-and-release system controlled by metamorphic conditions : Example from  
541 the Piedmont zone of the western Alps. *Chemical Geology*. In press.

542 Lardeaux, J.M., Schwartz, S., Paul, A., Tricart, P., Guillot, S., Béthoux, N., Masson, F., 2006.  
543 A crustal-scale cross section of the southwestern Alps combining geophysical and geological  
544 imagery. *Terra Nova* 18, 412-422.

545 Lemoine, M., Tricart, P., Boillot, G., 1987. Ultramafic and gabbroic ocean floor of the  
546 Ligurian Tethys (Alps, Corsica, Apennines): in search of a genetic model. *Geology* 15, 622-  
547 625.

548 Lewis, I., Chaffin, N., Gunter, M., Griffiths, P., 1996. Vibration spectroscopic studies of  
549 asbestos and comparison of suitability for remote analysis. *Spectrochimica Acta Part A* 52,  
550 315-328.

551 Li, X.P., Rahn, M., Bucher, K., 2004. Serpentinites of the Zermatt-Saas ophiolite complex  
552 and their texture evolution. *Journal of Metamorphic Geology* 22, 159-177.

553 Mellini, M., Ferraris, G., Compagnoni, R., 1985. Carlosturanite: HRTEM evidence of a  
554 polysomatic series including serpentine. *American Mineralogist* 70, 773-781.

555 Mével, C., Caby, R., Kienast, J.R., 1978. Amphibolite facies conditions in oceanic crust:  
556 example of amphibolitized flaser gabbros and amphibolites from the Chenaillet ophiolite  
557 massif (Hautes Alpes, France). *Earth and Planetary Science Letters* 39, 98-108.

558 Miyashiro, A., Shido, F., Ewing, M., 1969. Composition and origin of serpentinites from the  
559 Mid-Atlantic Ridge near 24 and 30°N. *Contribution to Mineralogy and Petrology* 23, 117-  
560 127.

561 O'Hanley, D.S., 1996. Serpentinites: Oxford Monographs on Geology and Geophysics 34,  
562 277p

563 Padron-Navarta, J.A., Sanchez-Vizcaino, V.L., Garrido, C.J., Gómez-Pugnaire, M.T.,  
564 Jabaloy, A., Capitani, G.C., Mellini, M., 2008. Highly ordered antigorite from Cerro del  
565 Almiraz HP-HT serpentinites, SE Spain. *Contribution to Mineralogy and Petrology* 156, 679-  
566 688.

567 Padron-Navarta, J.A., Hermann, J., Garrido, C.J., Sanchez-Vizcaino, V.L., Gómez-Pugnaire,  
568 M.T., 2010. An experimental investigation of antigorite dehydration in natural silica-enriched  
569 serpentine. *Contribution to Mineralogy and Petrology* 159, 25-42.

570 Perrillat, J.P., Daniel, I., Koga, K.T., Reynard, B., Cardon, H., Crichton, W.A., 2005. Kinetics  
571 of antigorite dehydration: A real-time X-ray diffraction study. *Earth and Planetary Science*  
572 *Letters* 236, 899-913.

573 Putnis, A., 2009. Mineral replacement reactions. *Reviews in Mineralogy and Geochemistry*  
574 70, 87-124.

575 Quirico, E., Montagnac, G., Rouzaud, J.N., Bonal, L., Bourrot-Denise, M., Dufer, S., Reynard,  
576 B., 2009. Precursor and metamorphic condition effects on Raman spectra of poorly ordered  
577 carbonaceous matter in chondrites and coals. *Earth and Planetary Science Letters* 287, 185-  
578 193.

579 Reynard, B., Wunder, B., 2006. High-pressure behavior of synthetic antigorite in the MgO-  
580 SiO<sub>2</sub>-H<sub>2</sub>O system from Raman spectroscopy. *American Mineralogist* 91, 459-462.

581 Rinaudo, C., Gastaldi, D., Belluso, E., 2003. Characterization of chrysotile, antigorite, and  
582 lizardite by FT-Raman spectroscopy. *Canadian Journal of Mineralogy* 41, 883-890.

583 Rosenbaum, G., Lister, G.S., 2005. The Western Alps from the Jurassic to Oligocene: spatio-  
584 temporal constraints and evolutionary reconstructions. *Earth Science Reviews* 69, 281-306.

585 Rüpke, L.H., Morgan, J.P., Hort, M., Connolly, J.A., 2004. Serpentine and the subduction  
586 water cycle. *Earth and Planetary Science Letters* 223, 17-34.

587 Scambelluri, M., Müntener, O., Hermann, J., Piccardo, G.B., Trommsdorff, V., 1995.  
588 Subduction of water into the mantle-history of an alpine peridotite. *Geology* 23, 459-462.

589 Schwartz, S., Tricart, P., Lardeaux, J.M., Guillot, S., Vidal, O., 2009. Final exhumation of an  
590 accretionary wedge (Queyras Schistes Lustrés, Western Alps): deformation sequence and  
591 associated P-T-t path. *Geological Society of America Bulletin* 121, 502-518.

592 Schwartz, S., Lardeaux, J.M., Tricart, P., Guillot, S., Labrin, E., 2007. Diachronous  
593 exhumation of subducted HP metamorphic rocks from southwestern Alps: evidences from  
594 fission-track analysis. *Terra Nova* 19, 133-140.

595 Schwartz, S., Allemand, P., Guillot, S., 2001. Numerical model of the effect of serpentinites  
596 on the exhumation of eclogitic rocks: insights from the Monviso ophiolitic massif (Western  
597 Alps). *Tectonophysics* 42, 193-206.

598 Schwartz, S., Lardeaux, J.M., Guillot, S., Tricart, P., 2000. The diversity of eclogitic  
599 metamorphism in the Monviso ophiolitic complex, western Alps, Italy. *Geodinamica Acta* 13,  
600 169-188.

601 Spear, F.S., 1993, *Metamorphic phase equilibria and pressure-temperature-time paths*:  
602 Washington, D.C., Mineralogical Society of America, 799 p.

603 Tricart, P., 1984. From passive margin to continental collision: A tectonic scenario for the  
604 western Alps. *American Journal of Science* 284, 97-120.

605 Tricart, P., Lemoine, M., 1986. From faulted blocks to megamullions and megaboudins-  
606 Tethyan heritage in the structure of the western Alps. *Tectonics* 5, 95-118.

607 Tricart, P., Schwartz, S., 2006. A north - south section across the Queyras Schistes lustrés  
608 (Piedmont zone, Western Alps): syncollision refolding of a subduction wedge. *Eclogae  
609 Geologicae Helvetiae* 99, 429-442.

610 Trommsdorff, V., Sanchez-Vizcaino, V.L., Gomez-Pugnaire, M.T., Müntener, O., 1998. High  
611 pressure breakdown of antigorite to spinifex-textured olivine and orthopyroxene, SE Spain.  
612 *Contribution to Mineralogy and Petrology* 132, 139-148.

613 Ulmer, P., Trommsdorff, V., 1995. Serpentinite stability to mantle depths and subduction  
614 related magmatism. *Science* 268, 858-861.

615 Wicks, F.J., O'Hanley, D.S., 1988. Serpentine minerals: Structures and petrology. *Rev  
616 Mineral*, 19, In S. W. Bailey Ed., *Hydrous Phyllosilicates*, pp. 91-167

617 Wunder, B., Schreyer, W., 1997. Antigorite: High Pressure stability in the system MgO-SiO<sub>2</sub>-  
618 H<sub>2</sub>O (MSH). Lithos 41, 213-227.

619

## Figure captions

Fig. 1. (a) Tectonic sketch map of the southwestern Alps, and  $T_{\max}$  results of metasediments obtained by the RSCM method. Seven serpentinites were sampled along the paleo-subduction zone from sub-greenschist (Chenaillet) to eclogitic (Monviso) facies conditions. (b) Characteristic evolution of Raman spectra from selected metasediments. Positions of the graphite G band and D1, D2, D3 defect bands are indicated. For each spectrum, the value of the mean R2 ratio ( $R2=D1/[G+D1+D2]$  peak area ratio) is given (see Table 1). (c)  $T_{\max}$  results projected onto a WSW – ENE cross section (XX').

Fig. 2. XRD patterns of serpentinites. The mineralogy is dominated by a magnetite and serpentine assemblage. The antigorite peaks (black star) and olivine (Ol) appear in samples RQ01 and Vi01. The presence of olivine is due to the onset of antigorite destabilization into olivine.

Fig. 3. Raman spectra acquired from different varieties of serpentine from the study area in low frequency ( $150-1150\text{ cm}^{-1}$ ) and OH stretching ( $3600\text{ to }3720\text{ cm}^{-1}$ ) ranges. The characteristic bands of antigorite ( $373, 1043, 3670\text{ and }3700\text{ cm}^{-1}$ ) and lizardite ( $390, 3680, 3703\text{ cm}^{-1}$ ) are indicated in grey. (a) Raman spectra of lizardite and chrysotile. (b) Raman spectra of antigorite related to the  $T_{\max}$ . (c) Raman spectra of mixed lizardite/antigorite serpentine.

Fig. 4. Photomicrographs of characteristic textures of serpentinite from the study area: Atg, antigorite; lz, lizardite; Chr, chrysotile; Mag, magnetite; x, polarized light; x', crossed-polarized light. The  $T_{\max}$  obtained from the associated metasediments is also indicated.

(a-a'). Sample ICH2 (Chenaillet massif). Mesh texture developed from olivine is observed in locations where lizardite is the only developed serpentine species. At the top of the image, secondary veins infilled by chrysotile cross-cut the mesh texture.

(b-b'). Sample CR02 comes from the low-temperature blueschist domain (Cristillan massif). The sample is dominated by mesh texture underlined by lizardite. Secondary antigorite crystallized at the boundary of the lizardite minerals. In the antigorite zone, relics of lizardite (brownish minerals) are still present.

(c-c'). Sample RQ23 comes from medium-temperature blueschist domain (Rocca Bianca massif). The sample is equally dominated by lizardite and antigorite. In the lizardite-dominant zone (greenish color), the mesh texture is partly preserved; however, antigorite developed at the expense of lizardite at the grain boundaries. Antigorite minerals with interlocked microstructures also form millimeter-sized patches that are free of lizardite relics.

(d-d'). Sample RQ16 comes from the intermediate-temperature blueschist domain (Refuge du Viso). The sample is dominated by antigorite minerals, which are developed in a dense network of veins at the expense of lizardite preserved in mesh texture.

Fig. 5. Photomicrographs of characteristic textures of serpentine species from the western Alps: Atg, antigorite; Lz, lizardite; Chr, chrysotile; Mag, magnetite; x, polarized light; x', crossed-polarized light. The  $T_{\max}$  obtain on the associated metasediments is also indicated.

(a-a'). Sample BB01 comes from the high-temperature blueschist domain (Bric Bouchet massif). This sample is dominated by antigorite. The magnetite underlines the early mesh structure.

(b-b'). Sample RQ01 comes from the high-temperature blueschist domain (Traversette massif). In this sample, only antigorite is observed. Mesh and bastite textures are well preserved, suggesting a static crystallization of antigorite, most likely at the expense of early lizardite produced during ocean floor metamorphism.

(c-c'). Sample Vi01 comes from Monviso eclogitic ophiolite. The antigorite is the only serpentinite species that preserves the mesh texture underlined by magnetite.

Fig. 6. Microprobe analyses (in weight %) of serpentinite samples plotted in an  $\text{Al}_2\text{O}_3$  versus  $\text{SiO}_2$  diagram (cf Table 3). The arrow indicates the metamorphic trend from sub-greenschist to eclogitic metamorphic facies conditions. The antigoritization processes in the serpentinites are characterized by a chemical homogenization associated with the increase in the metamorphic conditions.

Fig. 7. Idealized sketch determined from natural serpentinites that shows the evolution of the antigoritization processes under a HP metamorphic gradient. (a) Characteristic Raman spectra of serpentine species from the study area. The bands of antigorite (373, 1043, 3670 and 3700  $\text{cm}^{-1}$ ) are indicated in grey. (b) In sub-greenschist conditions, only lizardite is present. (c) In LT-blueschist, antigorite appears along the lizardite grain boundaries via a dissolution-precipitation process. (d) In MT-blueschist, the antigorite becomes the major phase. The veins of antigorite at the lizardite grain boundaries widen and the cores of lizardite show a mixed lizardite/ antigorite Raman spectra related to the onset of the solid-state transition. (e) In HT-blueschist, antigorite becomes the sole serpentine variety. Antigorite develops infra-millimetric blades superimposed over the original mesh texture.

Fig. 8. Phase diagram of antigorite and lizardite (after Evans, 2004): Lz, lizardite; Atg, antigorite; Chr, chrysotile; Fo, forsterite; Tlc, talc; Brc, brucite. Reactions (1) and (3) correspond to the onset of the reactions while (1') and (3') correspond to the end of these

reactions with the complete consumption of lizardite. Metamorphic facies are from Spear (1993). The natural stability field domain of coexisting lizardite and antigorite is restricted to a temperature range between ~320 and 390°C. At 390°C and above, the lizardite is entirely replaced by antigorite. Above 460°C, Reaction (4) results in the onset of crystallization of olivine. Between 320 and 390°C, the antigorite develops through Reaction (3) in the presence of SiO<sub>2</sub>-rich fluids by dissolution-precipitation processes. Between 340 and 380°C, Reaction (2) is also observed in the core of lizardite antigorite by solid-state transformation.

Table 1. RSCM results with longitude (Long.) and latitude (Lat.) in decimal degrees (WGS84), number of Raman spectra (n), R2 ratio (mean and standard deviation) and T<sub>max</sub> (mean and 1-σ uncertainty).

Table 2. Mineral assemblage of the studied serpentinites as detected by XRD, with (+ + +) major phase, (+) minor phase (<10%), and (-) absent or below detection limit (<1%). Facies metamorphic conditions and T<sub>max</sub> are also given. The black star indicates the presence of antigorite.

Table 3. Representative microprobe analyses of serpentine minerals from alpine serpentinites. All values are in wt% (b.d.l. = below detection limit; n.d. = not determined).